



The effects of Co/Ce co-doped ZnO thin films: an optical and defect study

L. Arda^{1,*}  and E. Ozugurlu²

¹ Department of Mechatronics Engineering, Faculty of Engineering and Natural Sciences, Bahcesehir University, 34349 Besiktas, Istanbul, Turkey

² Department of Mathematics, Istanbul Technical University, 34437 Maslak, Istanbul, Turkey

Received: 13 February 2025

Accepted: 27 April 2025

© The Author(s), 2025

ABSTRACT

Ce-doped ZnCoO ($\text{Zn}_{0.99-x}\text{Co}_{0.01}\text{Ce}_x\text{O}$) thin films (with $x = 0.00$ to 0.05 in increments of 0.01) were grown using the sol-gel technique to investigate the influence of defects on their optical properties. By applying a Double Facet Coated Substrate (DFCS) theoretical transmittance model to analyze the optical transmittance data, the thickness, absorption loss, extinction coefficient, and refractive index of the thin films were determined. The films' thicknesses and refractive indices ranged from 350 to 455 nm and 1.71 to 2.02 , respectively. The optical band gap fluctuates as the Ce concentration increases from 0.00 to 0.05 , and the extinction coefficient fluctuates with Ce concentration, and a maximum occurs at the 4% Ce concentration following the Sellmeier dispersion relation. However, the highest Urbach energy, 904 ± 613 meV, was observed for the 2% Ce-doped film. The photoluminescence (PL) spectra of Co/Ce co-doped ZnO thin films reveal the relative contributions of defects, namely Zn_i (zinc interstitials), V_{Zn} (zinc vacancies), and O_i (oxygen interstitials). X-ray diffraction (XRD) and scanning electron microscopy (SEM) were employed to analyze the structural properties and surface morphology of the films. Additionally, energy-dispersive spectroscopy (EDS) was used to determine the elemental composition of the thin films. This study demonstrates the effective use of the DFCS model to accurately determine the refractive index and extinction coefficient, two critical parameters for modeling photolithographic processes in the semiconductor industry.

1 Introduction

ZnO and doped ZnO nanomaterials have garnered significant attention due to their wide range of applications in fields such as biomedicine, pharmacy, spintronics, photocatalysis, semiconductor-based sensors, solar cells, LEDs, and photovoltaic systems [1–11]. The nearly universal use of ZnO can be attributed to its

advantageous properties, including low cost, high electron mobility, thermal stability, microwave absorption capabilities, infrared shielding, high exciton binding energy, wide bandgap, chemical resistance, optical transparency, photocatalytic efficiency, accessibility, non-toxicity, and tunable bandgaps [12–14]. Despite these superior properties, researchers have been actively working to enhance the structural, electrical,

Address correspondence to E-mail: lutfi.arda@bau.edu.tr

magnetic, and optical characteristics of ZnO by doping it with various elements, such as transition metals (e.g., Ni, Co, Fe, Mn) and rare earth elements (e.g., Y, Ce, Yb, Eu), to optimize its performance for specific applications [15–27]. Furthermore, ZnO nanomaterials—including nanoparticles, nanorods, and thin films—are synthesized using various physical and chemical methods, such as sol–gel, hydrothermal, coprecipitation, solid-state reaction, pulsed laser deposition, and DC sputtering, to further enhance their properties [28–34]. In both doping and the synthesis of ZnO nanomaterials, a key consideration is ensuring the material is single-phase, as well as investigating any defects that may arise during the process.

The ionic radius of the Co^{2+} ion is approximately 0.074 nm, which is comparable to that of the Zn^{2+} ion. Its electron configuration is $[\text{Ar}] 3d^7$, and due to the partially filled 3d orbitals, Co^{2+} exhibits d-d transitions in complexes formed with ligands. For this reason, Co^{2+} is a transition metal that has been widely incorporated into ZnO in various studies [32]. On the other hand, the ionic radius of the Ce^{3+} ion is approximately 0.102 nm (102 pm), which is larger than that of Zn^{2+} . Its electronic configuration is $[\text{Xe}] 4f^1$, and due to the involvement of f-orbitals, f-f transitions are very weak. As a result, the optical activity of the Ce^{3+} ion is lower compared to that of Co^{2+} . However, the Ce^{3+} ion can absorb UV light, making it a prominent candidate for UV protection. Some of the key findings from studies on Ce^{3+} in the literature are as follows: Satpathy et al. [33] reference the work of Chelouche et al. [2], who demonstrated that Ce doping reduces the UV and visible (green) emission intensity of ZnO nanofibers. They also found that increasing the Ce doping level from 0.1% to 0.9% significantly suppresses the emission intensity of ZnO thin films. Regarding the magnetic properties of Ce-doped ZnO, several studies have reported that ferromagnetic ZnO transitions to diamagnetic behavior at ambient temperature.

Moreover, Xin [34] observed that a decrease in Ce doping concentration led to a reduction in light transmittance within the wavelength range of 400 to 800 nm. Following Ce doping, the bandgap energy increased, resulting in improved optical properties suitable for the fabrication of ZnO heterostructured thin films. At room temperature, all films exhibited strong blue emission when excited at 375 nm, suggesting potential applications in optoelectronic devices. The UV–vis and photoluminescence (PL) spectra at ambient temperature revealed significant absorption in the near-UV

region, indicating enhanced absorption in the 370–400 nm range after Ce ion doping. As the Ce doping concentration increased, the optical transmittance of visible light decreased. Additionally, the bandgap energy increased with Ce doping. Notably, an intense blue emission with 89% color purity was observed under 375 nm excitation.

ZnO:Ce films hold potential for applications in near-ultraviolet (n-UV) LED light conversion materials and blue light sources. Building on this approach, doping ZnO nanomaterials with Co^{2+} and Ce^{3+} ions aims to introduce advanced functionalities and expand their utility across a wide range of optoelectronic applications, including solar cells, LEDs, photodetectors, spintronic devices, gas sensors, photocatalysts, IR detection systems, and laser technologies. By experimentally and theoretically optimizing the optical and electronic properties achieved through this doping, the goal was to enhance the performance of these technologies [35–37].

In this work, zinc oxide films co-doped with cobalt and cerium were fabricated using the sol–gel dip-coating process. Five distinct $\text{Zn}_{0.99-x}\text{Co}_{0.01}\text{Ce}_x\text{O}$ thin films were produced by varying the cerium content from 0.01 to 0.05, and their optical transmittance was measured in the wavelength range of 200 to 1100 nm. The selection of cerium doping was primarily influenced by the four resonant absorption peaks observed. To identify the optimal configuration for maximum performance, the optical properties of the thin films—such as the refractive index and extinction coefficient—were analyzed and evaluated for different cerium doping ratios. For this purpose, parametric equations for the thin film's transmittance, extinction coefficient, and refractive index were developed. Using the mathematical model (the DFCS transmittance model) proposed in [36], we numerically computed the parameters of Cauchy's three-term dispersion equation and four distinct Lorentzian absorption profiles through the least-squares approach.

2 Experimental

2.1 Production of thin films

The DFCS samples were fabricated by depositing Co/Ce-doped ZnO thin films on soda-lime glass (SLG) substrates using the sol–gel process to experimentally validate our methodology. Zinc acetate dihydrate

(ZnAc) (Sigma Aldrich, 99–102%), cobalt acetate tetrahydrate (CoAc) (Alfa Aesar, 98–102%), and cerium acetate tetrahydrate (CeAc) (Sigma Aldrich, 99.9%) were used as starting materials, with methanol (ME) and monoethanolamine (MEA) serving as solvents and stabilizers, respectively. To maintain a 1:1:1 molar ratio of ZnAc:CoAc:CeAc:MEA, we dissolved ZnAc, CoAc, and CeAc in ME at a concentration of 0.25 M and then added MEA to the mixture. The final solution was continuously stirred at room temperature using a magnetic stirrer until a transparent solution was obtained. The pH of the solutions was measured using a standard pH meter. The viscosities of the solutions were adjusted by adding ME, and the detailed procedures are provided in [18, 21].

To achieve high-quality thin films, it is essential to prepare the pristine SLG substrates as thoroughly as possible. First, the SLG substrates were washed with detergent, rinsed with purified water, and then sonicated for 5 min in a 20% sulfuric acid/purified water solution. Finally, the substrates were rinsed again with purified water and dried using a nitrogen flow. This cleaning process effectively removed all contaminants from the surface of the SLG substrates. After cleaning, the substrates were dipped into the Co/Ce co-doped ZnO solutions and then pulled through a vertical furnace at 400°C. The thickness of the films was controlled by adjusting the number of dips, the withdrawal rate, and the solution dilution. This process was repeated until the desired film thickness was achieved, ensuring a thick and uniform coating. Subsequently, the glass substrates and thin films were annealed at 600°C for 30 minutes to form a crystalline structure.

2.2 Characterization of Co/Ce co-doped ZnO thin films

The Co/Ce co-doped ZnO thin films were characterized using a Shimadzu UV mini 1240 UV/Vis/NIR spectrophotometer and a scanning electron microscope (SEM) (JEOL, JSM-5910LV). X-ray diffraction (XRD) patterns were obtained using a Rigaku Multiflex diffractometer with Cu K α radiation ($\lambda = 1.5408 \text{ \AA}$). The 2θ range of 20° to 80° was scanned, with increments of 0.02 and a scanning speed of 3°/min. The $\text{Zn}_{0.99-x}\text{Co}_{0.01}\text{Ce}_x\text{O}$ ($x = 0.00\text{--}0.05$) thin films, produced in polycrystalline form via the sol–gel technique, were further analyzed for their

photoluminescence properties using an Agilent Cary Eclipse Fluorescence Spectrophotometer.

2.3 The equations of transmittance model

The sol–gel dip-coating process produces a thin layer on both sides of the substrate, similar to the Langmuir–Blodgett and chemical bath deposition (CBD) techniques [36]. As a result, two symmetric thin films form on opposite sides of the substrate, as illustrated in Fig. 1b. In our earlier research, this structure was referred to as a “Double Facet Coated Substrate” (DFCS), whereas a conventional film deposited on a single side of the substrate was termed a “Single Facet Coated Substrate” (SFCS) (Fig. 1a) [36]. The presence of the second thin layer creates a fundamentally different interaction between light and the DFCS compared to the SFCS. Consequently, the widely used envelope method (Swanepoel’s method) for analyzing thin films on a substrate cannot be directly applied to DFCS systems.

The electric field reflection and transmission coefficients for an air-film-substrate (afs) system are provided as follows, respectively, for the equation of the double-facet-coated substrate system of transmittance in Sec. 2.1 [36]:

$$r_{afs} = \frac{r_{af} + r_{fs} \exp(i\theta)}{1 + r_{af}r_{fs} \exp(i\theta)}, \quad t_{afs} = \frac{t_{af} + t_{fs} \exp(i\theta)}{1 + r_{af}r_{fs} \exp(i\theta)} \quad (1)$$

where $\theta = 4\pi\eta_{film}d_{film}/\lambda$ is the complex phase shift at each round trip through the film of thickness d_{film} at the wavelength λ , and η_{film} is the complex refractive index of the thin film (af: air-film, fs: film-substrate). However, since the intensity reflectance (R_{afs}) and transmittance (T_{afs}) are real quantities that can be

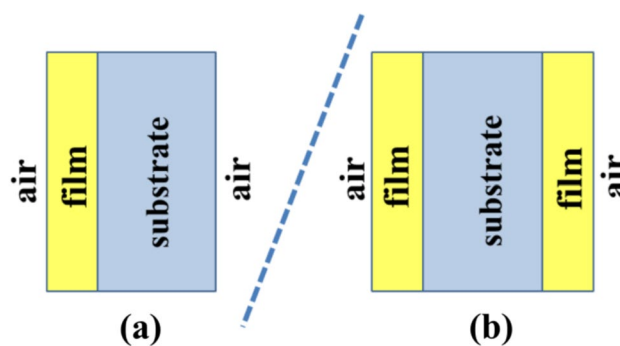


Fig. 1 **a** Single Facet Coated Substrate (SFCS), **b** Double Facet Coated Substrate (DFCS) [36]

measured directly, these are the parameters most relevant to experiments:

$$R_{afs} = r_{afs}r_{afs}^*, \quad T_{afs} = \frac{n_a}{n_s}t_{afs}t_{afs}^* \tag{2}$$

where n_a and n_s are the refractive indices of air and substrate, respectively, and * operator denotes the complex conjugate.

It is important to note that these equations assume a semi-infinite substrate thickness, meaning the transmitted light remains confined within the substrate medium. For a substrate with finite thickness, the well-known Swanepoel’s formula [36] is used to describe the transmittance T_{afs} .

As in our previous work [36], we investigated the transmittance using a broadband light source with a short coherence length comparable to the thickness of the thin films. Consequently, the phase shift of the electric field induced by the film thickness must be taken into account, as the reflectance and transmittance formulas for zones 1 and 3 depend on the coherent summation of the multiple reflected electric fields. However, there will be no interference between the various reflected electric fields, as the thickness of region 2 (the substrate) is significantly larger than the coherence length of the light source. Consequently, the effect of the finite substrate is determined by the sum of the multiple reflected intensities rather than the coherent summation of the electric fields. Nevertheless, we account for the substrate thickness in our calculations because it influences the extent of light beam attenuation [36]. Equation (2) provides the

transmittance, T_{afs} , and the infinite coherent summation in the first phase-dependent thin film is illustrated in Fig. 2. As described in Sec. 2.1 [36], the total transmittance of this DFCS system can be determined by summing these coefficients:

$$T_{system} = T_{afs}UT_{sfa}(1 + U^2R_{sfa}^2 + U^4R_{sfa}^4 + U^6R_{sfa}^6 + \dots) \tag{3}$$

Given that $|U^2R_{sfa}^2| < 1$, the geometric series expansion formula can be used to reduce the above equation as follows :

$$T_{system} = \frac{T_{afs}T_{sfa}U}{1 - R_{sfa}^2U^2} \tag{4}$$

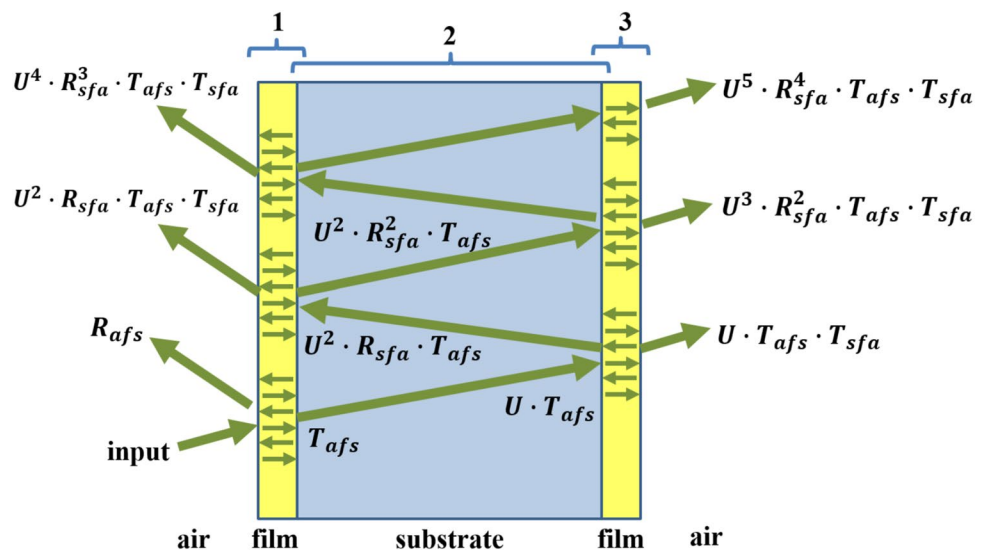
where the absorption loss is $U = e^{-\alpha_{sub}d_{sub}}$, the absorption coefficient of the substrate is α_{sub} , $\alpha_{sub} = \frac{4\pi}{\lambda}k_{sub}$, the extinction coefficient of the substrate is k_{sub} , the substrate thickness is d_{sub} , the reflection coefficient is R_{sfa} , the afs transmittance is T_{afs} , and the sfa transmittance is T_{sfa} .

It is important to note that when $U = 1$ in Eq. (4), corresponding to a lossless substrate, the improved Swanepoel’s formula, as derived in our previous work [12], is obtained. Similarly, the total reflectance R_{system} of the DFCS system is provided in Sec. 2.1 [36] as:

$$R_{system} = R_{afs} + \frac{T_{afs}T_{sfa}R_{sfa}U}{1 - R_{sfa}^2U^2} \tag{5}$$

Equation (4) was used to determine η_{film} , U , and d_{film} . The refractive index of the thin film was

Fig. 2 The DFCS system’s total transmittance formula’s derivation [36]



calculated using a three-term Cauchy dispersion relation, expressed as follows:

$$n_{film} = A + \frac{B}{\lambda^2} + \frac{C}{\lambda^4} \tag{6}$$

Similarly, the extinction coefficients of these films were determined using four distinct Lorentzian absorption profiles and a wavelength-independent term, as described below:

$$k_{film} = \frac{D}{1 + \left(\frac{\lambda - \lambda_D}{w_D}\right)^2} + \frac{E}{1 + \left(\frac{\lambda - \lambda_E}{w_E}\right)^2} + \frac{F}{1 + \left(\frac{\lambda - \lambda_F}{w_F}\right)^2} + \frac{G}{1 + \left(\frac{\lambda - \lambda_G}{w_G}\right)^2} + H \tag{7}$$

where the amplitudes of the Lorentzian peaks: D, E, F and G , the resonance wavelengths: $\lambda_D, \lambda_E, \lambda_F$ and λ_G , the absorption widths w_D, w_E, w_F , and w_G . Here, H is the white loss term. The first three peaks (D, E, F) are chosen to model the three resonant low absorption peaks of cobalt as stated in Sect. 2.2 in [36]. The fourth peak (G) was included to explain the heavy loss at shorter wavelengths. Due to the negligible total loss within the wavelength range of interest, the Kramers-Krönig relation between η_{film} and k_{film} was disregarded in this study. The refractive index of soda-lime-silica glass (SLSG) was provided by Rubin as [31]:

$$n_{sub} = \sqrt{1.513 - 3.169 \times 10^{-3} \lambda^{-2} + \frac{3.962 \times 10^{-3}}{\lambda^2}} \tag{8}$$

Equation (4) provides the transmittance of an uncoated substrate if the film thickness $d_{film} = 0$ or $\eta_{film} = \eta_{air}$. Based on our earlier computations [36], the absorption loss U equation is as follows:

$$U = \frac{-T_{as}^2 + \sqrt{T_{as}^4 + 4R_{as}^2 T_{sub}^2}}{2R_{as}^2 T_{sub}} \tag{9}$$

where T_{sub} is the experimental transmittance data of the uncoated substrate, R_{as} is the air-substrate interface reflectance, and T_{as} is the air-substrate interface transmittance. Figure 3 shows T_{sub} as a function of wavelength. After calculating U , the previously mentioned equation $U = e^{-\alpha_{sub} \cdot d_{sub}}$ can be applied to get k_{sub} . With a caliper, d_{sub} was discovered to be 1240 μm . Equation (4) can be solved by substituting $n_{film}, k_{film}, n_{sub}$, and k_{sub} . This leaves T_{system} with 10 unknown parameters (6 from k_{film} , 3 from n_{film} , and d_{film}).

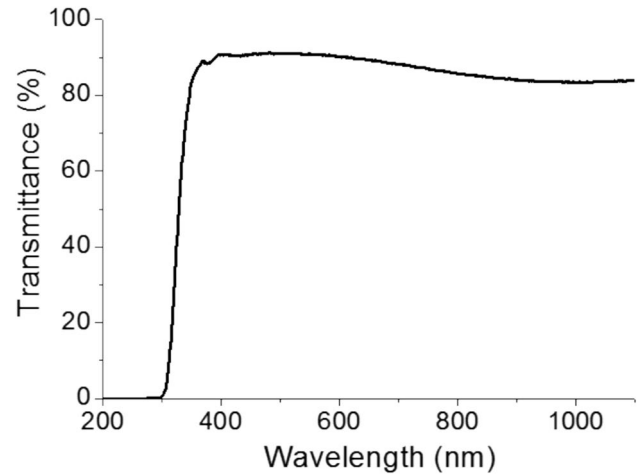


Fig. 3 Uncoated SLSG substrate optical transmittance [36]

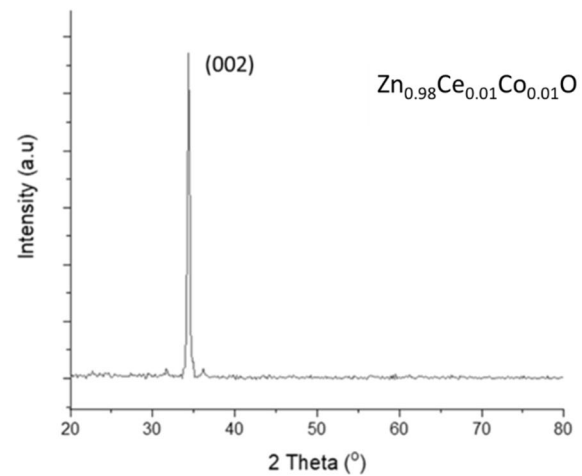


Fig. 4 $\text{Zn}_{0.98}\text{Ce}_{0.01}\text{Co}_{0.01}\text{O}$ thin film: single-phase XRD pattern

3 Results and discussion

3.1 Analysis of structural characterization

Figure 4 shows the X-ray diffraction (XRD) scan of the $\text{Zn}_{0.99-x}\text{Co}_{0.01}\text{Ce}_x\text{O}$ thin film deposited on a glass substrate. The XRD pattern reveals a c-axis-oriented (002) peak at $2\theta = 34.50^\circ$, confirming the formation of a single-phase hexagonal wurtzite structure (ICDD card No. 36-1451) belonging to space group P63 mc without any secondary phases associated with CoO or CeO.

3.2 The features of morphology

The SEM images reveal that the $\text{Zn}_{0.99-x}\text{Co}_{0.01}\text{Ce}_x\text{O}$ thin film has surfaces covered with small particles, as shown in Fig. 5a–b. Additionally, the thin film was found to be free of pinholes and cracks. The thickness of the $\text{Zn}_{0.98}\text{Ce}_{0.01}\text{Co}_{0.01}\text{O}$ thin film, determined from the cross-sectional SEM image (Fig. 5b), was approximately 420 nm, with relative errors ranging from 4×10^{-3} to 6×10^{-3} . These computed thickness values are consistent with our experimental findings. The elemental composition of the $\text{Zn}_{0.98}\text{Ce}_{0.01}\text{Co}_{0.01}\text{O}$ thin film was analyzed using energy-dispersive spectroscopy (EDS), which shows distinct peaks for zinc, cerium, cobalt, and oxygen in Fig. 5c. This confirms that the components of the film match the intended composition used during its fabrication.

3.3 Photoluminescence (PL)

Photoluminescence (PL) spectra provide valuable insights into the crystalline characteristics, defect types, and defect densities of semiconductor materials. To investigate the effects of Ce doping on the crystalline properties, defect types, and defect densities of ZnO thin films, we conducted PL analysis. The analysis revealed two distinct emission peaks: a strong ultraviolet (UV) emission peak and a broad visible emission band. These peaks are significant as they are characteristic of n-type ZnO semiconductors. The visible emission band can be divided into two regions: the first region exhibits violet to orange emission, while the second region shows red emission. It is widely accepted that the UV emission reflects the quality and quantity of defects in ZnO, whereas the visible emission is associated with the presence of defects [38–40].

The UV emission is typically associated with the near-band-edge (NBE) transition, an optical

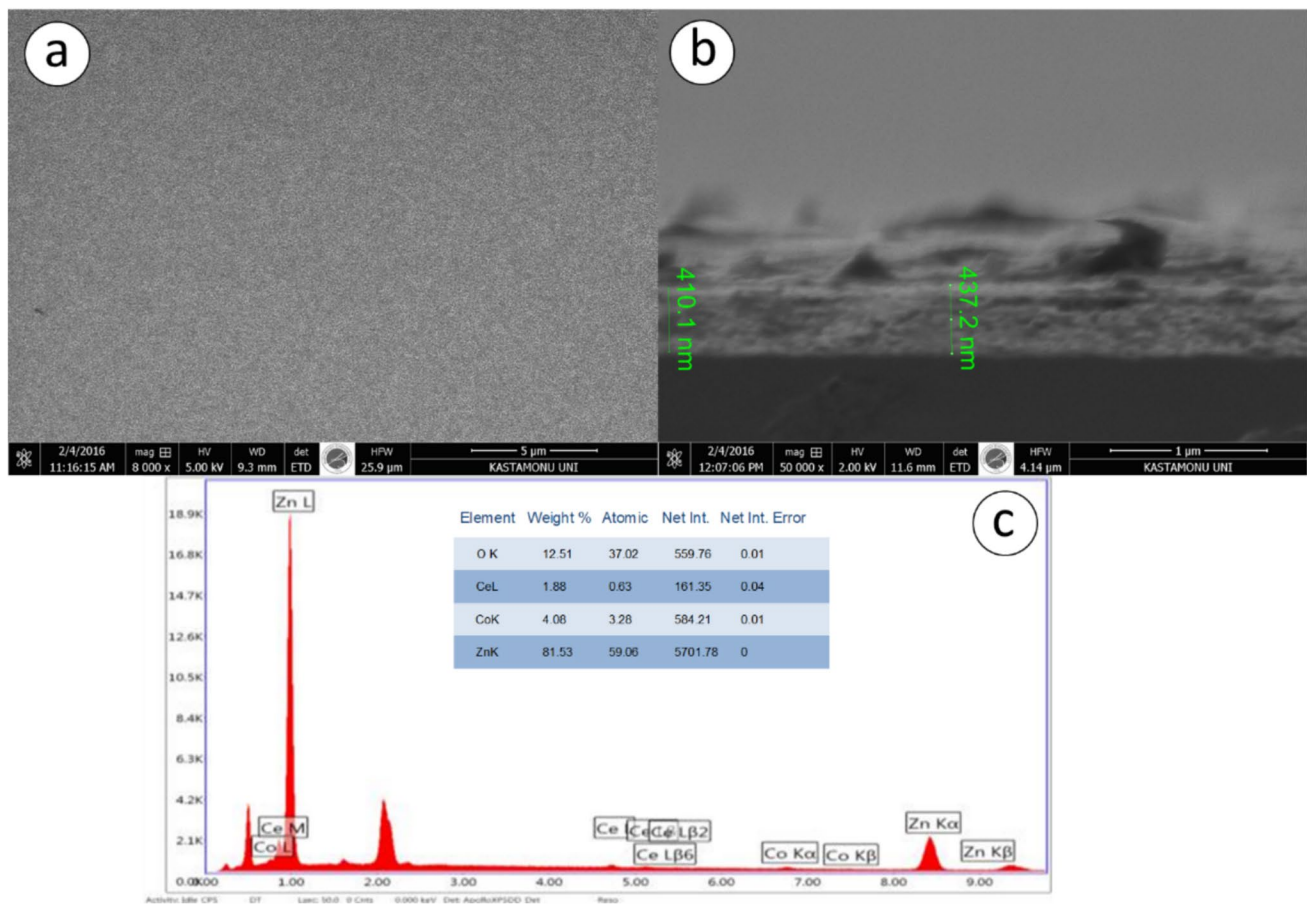


Fig. 5 $\text{Zn}_{0.98}\text{Ce}_{0.01}\text{Co}_{0.01}\text{O}$ thin films **a** SEM image **b** cross section and **c** EDS image

characteristic of ZnO’s wide bandgap. NBE emission arises from excitonic transitions between holes in the valence band and electrons in the conduction band [40]. Stronger UV emission is generally observed in ZnO materials with higher crystallinity and fewer defects. The stability of NBE emission has been consistently demonstrated in previous studies [40]. An annealing temperature of 600 °C is considered optimal, as it also promotes the formation of a high-quality crystal structure.

Notably, the visible emission band is divided into two distinct regions. The first region covers violet, blue, green, yellow, and orange wavelengths, while the second region spans red and near-infrared (NIR) wavelengths. These visible emissions, often referred to as deep-level (DL) emissions, are attributed to impurities or defects in the ZnO crystal lattice, such as oxygen antisites (O_{Zn}), zinc interstitials (Zn_i), oxygen vacancies (V_o), and oxygen interstitials (O_i) [38–40]. Emission peaks have been observed in the violet, blue, green, yellow, red, and near-infrared regions. To better understand the defects responsible for these emissions, the PL spectra were analyzed using Gaussian decomposition. This method was applied to investigate the structural defects in Co/Ce co-doped ZnO thin films.

The spectral curves were determined using the following model, and the decomposition was performed using the Fityk software:

$$f(\lambda) = ae^{-(\lambda-b)^2/2c^2} \tag{10}$$

Using Fityk software, the analysis of the photoluminescence (PL) spectra related to Ce content revealed 13 main Gaussian decompositions, as shown for $Zn_{0.99-x}Co_{0.01}Ce_xO$ ($x = 0.0-0.05$) films in Fig. 6. The figure displays the areas and central positions of each peak. These peaks correspond to ultraviolet (UV), violet, blue, red, and near-infrared (NIR) emissions (Peaks 1–13). The emission regions are described as follows: (a) UV emissions (362–380 nm) region: these are attributed to the near-band-edge (NBE) transitions of Co/Ce co-doped ZnO, exhibiting excitonic characteristics; (b) Violet emissions (308–450 nm): these result from electron transitions from zinc interstitials (Zn_i) to the valence band; (c) Blue emissions (450–500 nm) region: these are associated with zinc vacancies (V_{Zn}); (d) Red emissions (670–750 nm) region: these are linked to oxygen interstitials (O_i); (e) Near-infrared (NIR) emissions (750–826 nm) region: these are attributed

to secondary UV diffraction and are likely caused by oxygen vacancies, as reported by Arda et al. [40].

The areas of the observed peaks were calculated to identify the dominant defects, as a larger peak area indicates a higher concentration of defects [40]. The percentages under the Gaussian curves for each Ce concentration were also determined. The PL spectra of Co/Ce co-doped ZnO thin films provide the relative percentages of defects, emission ranges, emission origins, and peak positions, as summarized in Table 1.

Figure 6 illustrates the distribution of defects in $Zn_{0.99-x}Co_{0.01}Ce_xO$ ($x = 0.0-0.05$) films using pie charts based on the Ce doping ratio. Three emission regions—violet, blue, and red—were observed in Fig. 6, corresponding to zinc interstitials (Zn_i), zinc vacancies (V_{Zn}), and oxygen interstitials (O_i), respectively. The violet region exhibited the highest emission intensity, suggesting a predominance of Zn_i defects. Emissions in the red region are associated with divalent oxygen vacancies (V_o^{++}) between 620 and 670 nm and interstitial oxygen (O_i) between 670 and 750 nm [40]. However, while O_i defects varied with Ce concentration, V_o^{++} defects were not observed in Fig. 6.

3.4 Fitting non-linear curves using transmittance data

Since thin films exhibit significant optical loss below this range, we considered the wavelength range of 200–1100 nm in our calculations. Figure 7 shows the transmittance values for five distinct $Zn_{0.99-x}Co_{0.01}Ce_xO$ thin films ($x = 0.01-0.05$). In the visible range of 400–700 nm, the films demonstrated optical transparency exceeding 75%, indicating high transparency in this region. These exceptional transmittance properties make the films suitable materials for optical coatings. To determine the unknowns, \vec{x} , that minimize the resulting quantity, we developed an optimization code using the Nelder-Mead simplex method in MATLAB.

$$\min_{\vec{x}} \sum_{i=1}^N T_{system}(\vec{x}, \lambda_i) - T_i^2 \tag{11}$$

where T_i : the observed transmittance data and λ : wavelength data. $T_{system}(\vec{x}, \lambda_i)$ was defined in Eq. (4), where N is the number of data points. \vec{x} comprises 10 unknown entries, specifically 3 parameters from n_{film} , 6 parameters from k_{film} , and d_{film} that require optimization. Assuming a wavelength-independent refractive

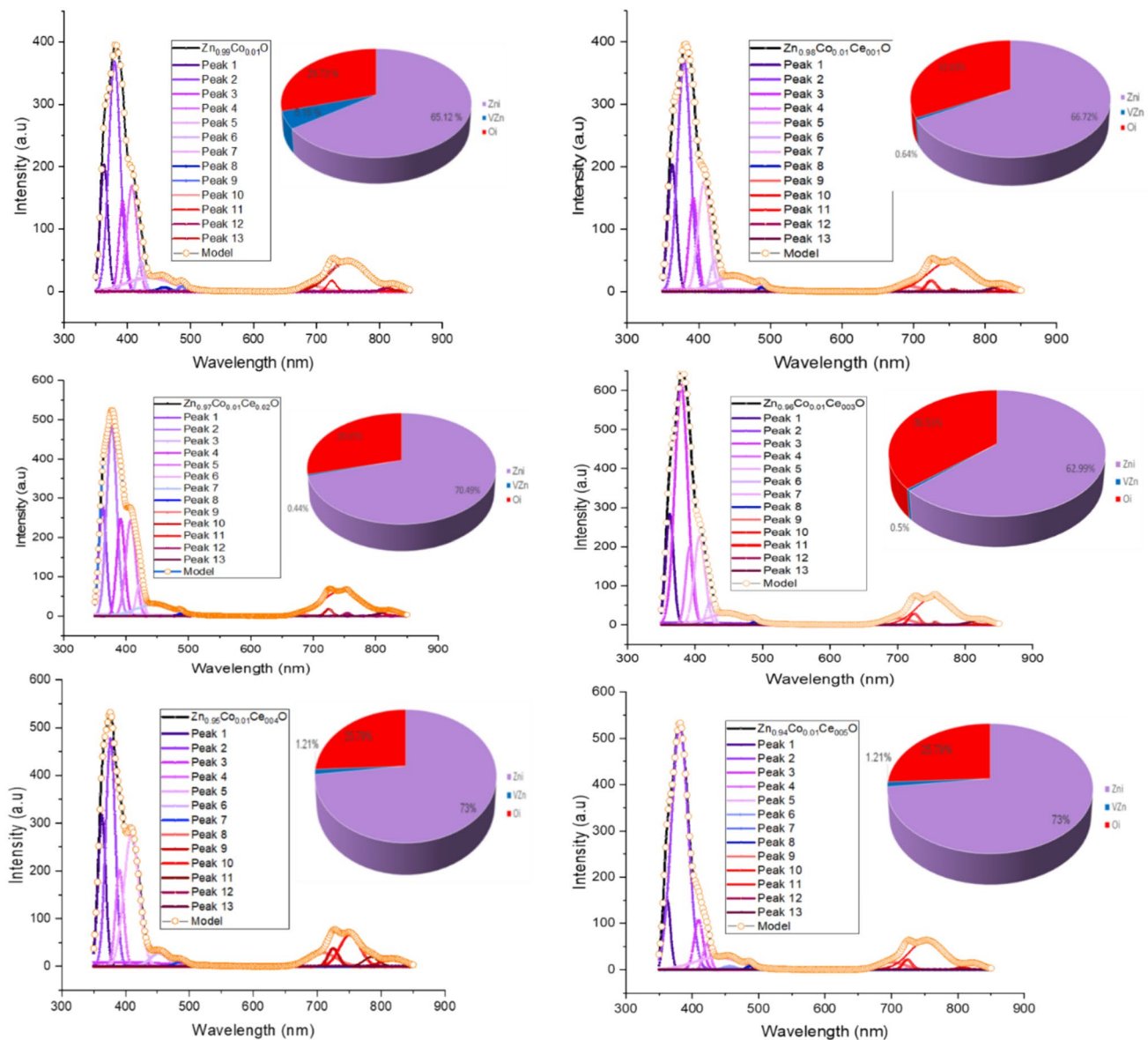


Fig. 6 Gaussian decompositions of the PL spectra of $Zn_{0.99-x}Co_{0.01}Ce_xO$ ($x = 0.0-0.05$) films were performed using Fityk software, and the relative percentages of each point defect observed at each Ce concentration are displayed in a pie chart in the inset

Table 1 PL spectra of Co/Ce co-doped ZnO thin films using Fityk software to determine the proportional proportions of defects, emission ranges, emission origins, and peak areas using the Gaussian distribution

	Ce concentration (%)						Wavelength range (nm)	Emission Range	Surface defects	
	0	1	2	3	4	5				
Area under curve (%)	65.12	66.72	70.49	62.99	73.00	45.92	380–450	Violet	$(Zn_i) \rightarrow (V_B)$	DL
	5.16	0.64	0.44	0.50	1.21	4.53	450–500	Blue	(v_{Zn})	Emission
	29.73	32.63	29.07	36.51	25.79	49.55	670–750	Red	(O_i)	

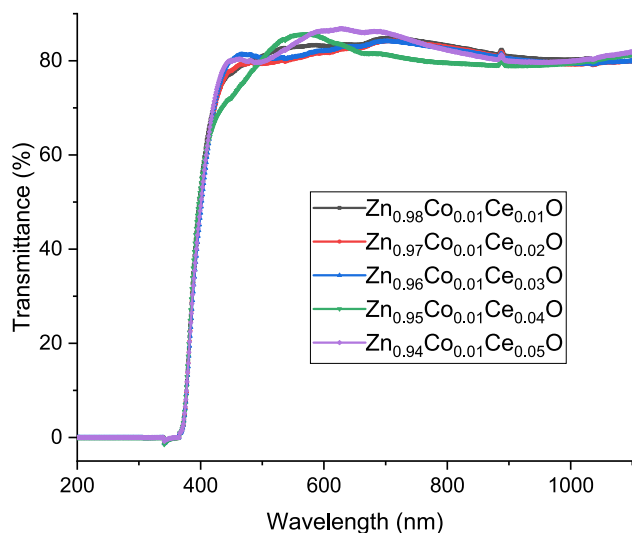


Fig. 7 $Zn_{0.99-x}Co_{0.01}Ce_xO$ ($x = 0.01-0.05$) thin films: experimental transmittance vs. wavelength

index and loss, the initial values of these 10 parameters were determined for the curve-fitting problem. Figure 8 shows the curve-fitting models after the optimized 10 unknowns were identified.

Figure 9a–e display the theoretical curve fits and experimental transmittance data plotted against wavelength, along with their corresponding magnified graphs. The small peaks observed at 900 nm in all plots (Fig. 9a–e) are attributed to the substrate, as previously discussed in our earlier study [36]. Additionally, our model utilized the experimental data to estimate the substrate loss.

The curve-fitting model employed the Nelder-Mead simplex technique to determine the optimal values for

the 10 unknowns, as listed in Table 2. Additionally, the relative error for each fitting was calculated using the following formula:

$$\sqrt{\sum \left(\frac{|ExperimentalData - CurveFitting|}{|ExperimentalData|} \right)^2} \quad (12)$$

which is shown in Table 2.

3.5 Extinction coefficient and dispersion relation

Figures 10 and 11 illustrate the extinction coefficient and the dispersion relation versus wavelength λ (Eq. (6) and Eq. (7)), respectively, for each thin film. Figure 10 reveals an oscillating trend in the extinction coefficient k_{film} as the Ce concentration increases, as determined by Eq. (7) using the data from Table 2. This trend aligns with Sellmeier’s dispersion relation, except for the 4% Ce concentration, where the extinction coefficient k_{film} reaches a maximum value of approximately 0.16. This peak correlates directly with enhanced radiative losses, indicating dominant scattering phenomena in the medium at this concentration [41]. Additionally, as shown in Fig. 11, the refractive index values typically range from 1.71 to 2.02, which aligns with the findings of Karakaya and Kaba [8]. For a Ce concentration of 3%, higher refractive index values are observed at wavelengths $\lambda > 850$ nm.

As seen in Fig. 11, the refractive index ranges from 1.71 to 2.02. Especially, the $Zn_{0.95}Co_{0.01}Ce_{0.03}O$ film, with a refractive index range of 2.01–2.02, is suitable for optoelectronic applications such as solar cells and

Fig. 8 $Zn_{0.99-x}Co_{0.01}Ce_xO$ ($x = 0.01-0.05$) thin films: approximated transmittance vs. λ

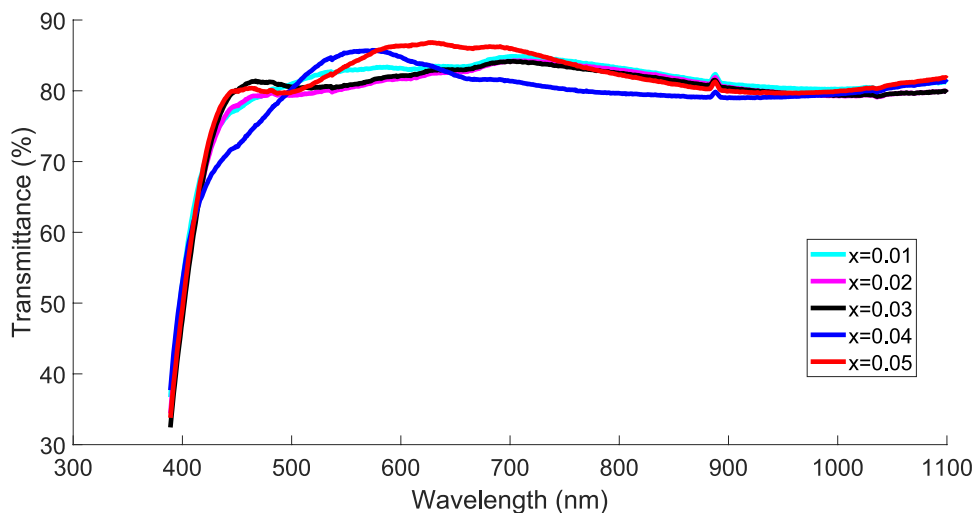


Fig. 9 **a** $\text{Zn}_{0.99-x}\text{Co}_{0.01}\text{Ce}_x\text{O}$ thin films: $x = 0.01$ and its zoomed graphs for the theoretical curve fits (in red) versus λ and experimental transmittance measurements (in black). **b** $\text{Zn}_{0.99-x}\text{Co}_{0.01}\text{Ce}_x\text{O}$ thin films: $x = 0.02$ and its zoomed graphs for the theoretical curve fits (in red) versus λ and experimental transmittance measurements (in black). **c** $\text{Zn}_{0.99-x}\text{Co}_{0.01}\text{Ce}_x\text{O}$ thin films: $x = 0.03$ and its zoomed graphs for the theoretical curve fits (in red) versus λ and experimental transmittance measurements (in black). **d** $\text{Zn}_{0.99-x}\text{Co}_{0.01}\text{Ce}_x\text{O}$ thin films: $x = 0.04$ and its zoomed graphs for the theoretical curve fits (in red) versus λ and experimental transmittance measurements (in black). **e** $\text{Zn}_{0.99-x}\text{Co}_{0.01}\text{Ce}_x\text{O}$ thin films: $x = 0.05$ and its zoomed graphs for the theoretical curve fits (in red) versus λ and experimental transmittance measurements (in black)

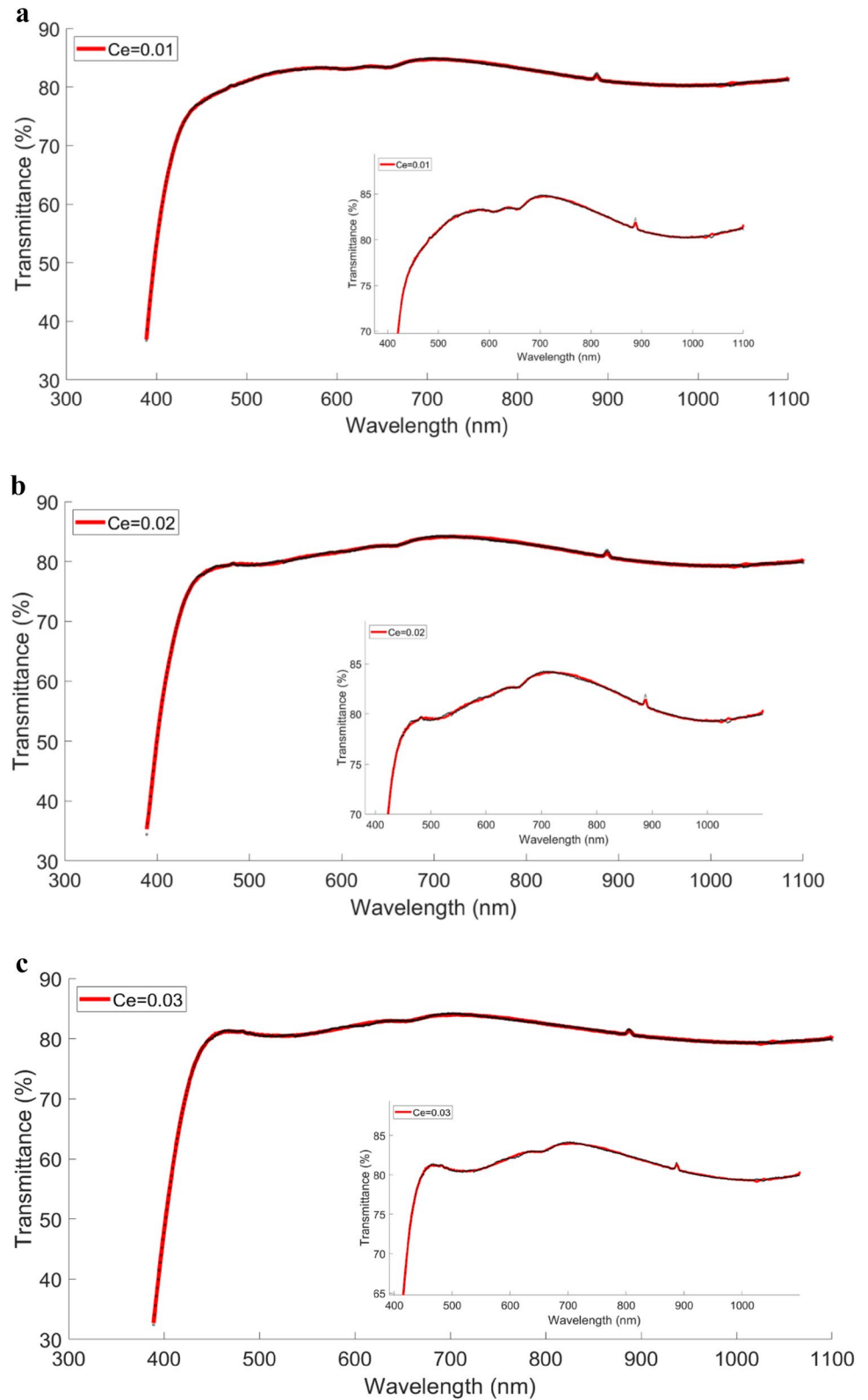
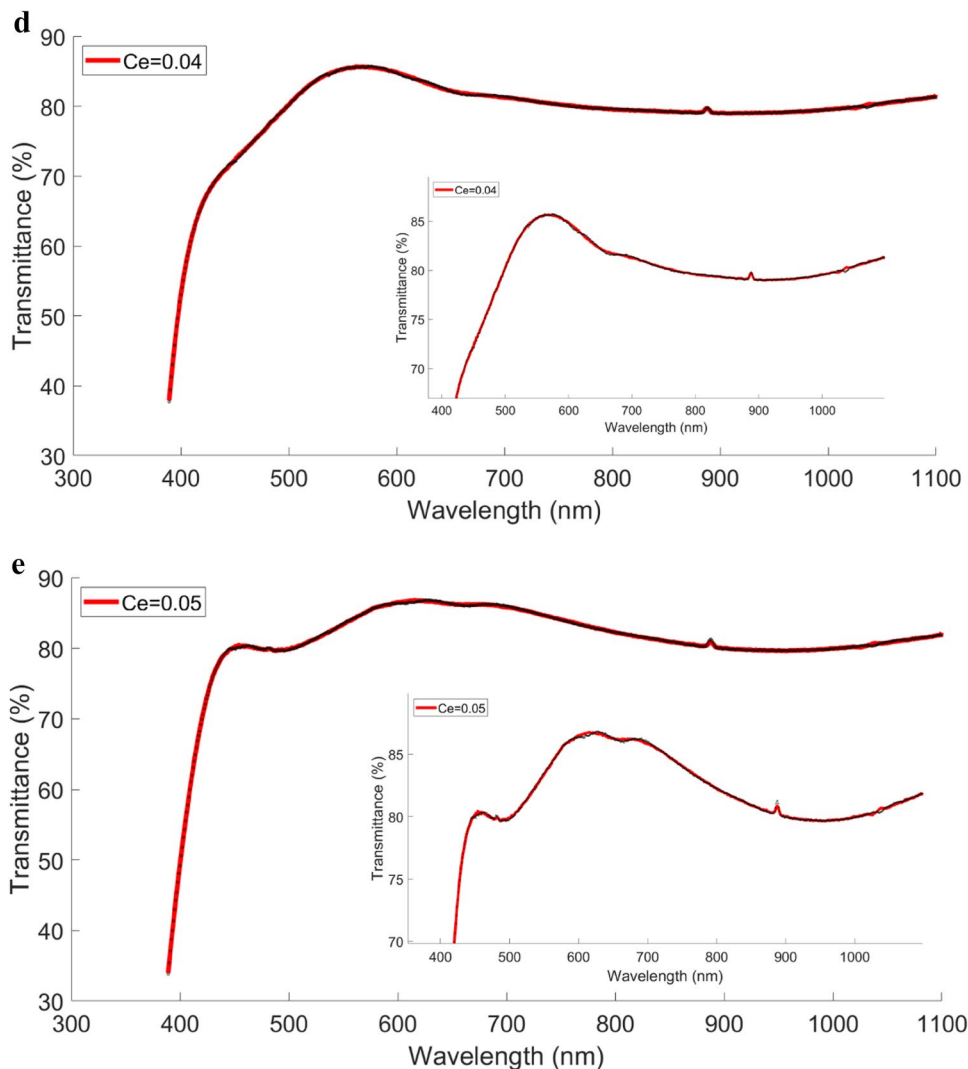


Fig. 9 continued



LEDs. However, in the IR region, $Zn_{0.99-x}Co_{0.01}Ce_xO$ ($x = 0.01, 0.02, 0.04,$ and 0.05), with refractive index values of 1.71 to 1.81 (approximately 2.0 or lower), were found to be appropriate for applications in IR sensors, optical filters, and photodetectors.

3.6 Band gap calculation

The optical band gap E_g can be found using the formula between the absorption coefficient (α) and photon energy ($h\nu$) as follows:

$$\alpha h\nu = k(h\nu - E_g)^{1/n} \tag{13}$$

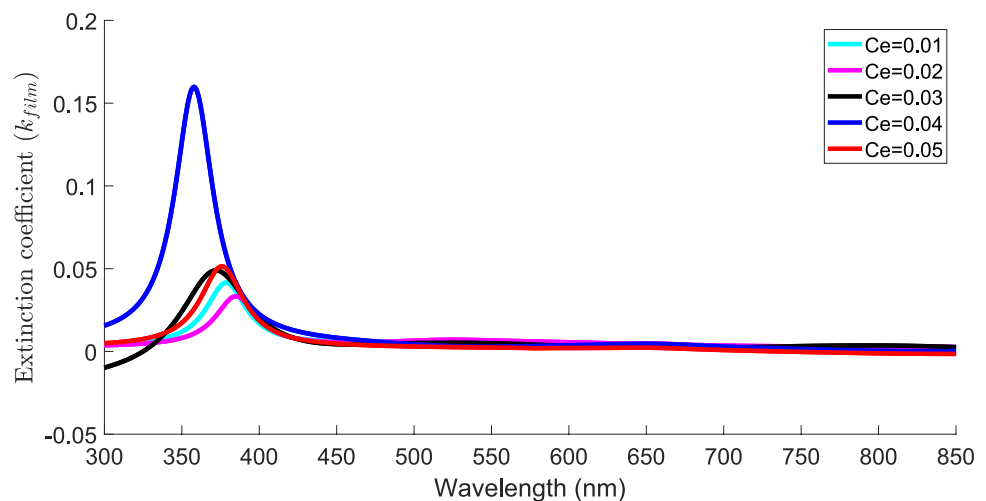
where h is the Plank’s constant, ν is the frequency of the vibration, and k is a constant. The exponent n depends on the type of the transition and takes the value $1/2$ for the indirect transitions, while 2 for the direct allowed transitions [42, 43].

In Eq. (13), E_g and k stand for the optical band gap and energy-independent constants, respectively. Since ZnO has direct-permitted transitions and $F(R_\alpha)$ is proportional to α , n is assumed to be 2. Consequently, Eq. (13) can be changed to:

$$F(R_\alpha)h\nu = k(h\nu - E_g)^{1/2} \tag{14}$$

Table 2 $\text{Zn}_{0.99-x}\text{Co}_{0.01}\text{Ce}_x\text{O}$ thin films ($x = 0.01\text{--}0.05$): sixteen optimized curve-fitting model parameters and the relative errors

	$\text{Zn}_{0.98}\text{Ce}_{0.01}\text{Co}_{0.01}\text{O}$	$\text{Zn}_{0.97}\text{Ce}_{0.02}\text{Co}_{0.01}\text{O}$	$\text{Zn}_{0.96}\text{Ce}_{0.03}\text{Co}_{0.01}\text{O}$	$\text{Zn}_{0.95}\text{Ce}_{0.04}\text{Co}_{0.01}\text{O}$	$\text{Zn}_{0.94}\text{Ce}_{0.05}\text{Co}_{0.01}\text{O}$
A	1.714	1.753	2.014	1.763	1.747
B	-0.138	-0.170	-0.240	-0.082	-0.084
C	0.021	0.026	0.029	0.011	0.014
D	0.003	0.003	0.001	-0.003	0.000
E	0.001	0.002	0.028	-0.007	-0.005
F	0.001	0.001	0.020	0.002	0.001
G	0.038	0.030	0.059	0.154	0.049
w_D (μm)	0.103	0.050	0.020	0.071	0.008
w_E (μm)	0.027	0.089	0.273	0.182	0.180
w_F (μm)	0.018	0.014	-0.155	0.041	0.038
w_G (μm)	0.016	0.016	-0.027	0.015	0.017
λ_D (μm)	0.508	0.520	0.656	0.532	0.579
λ_E (μm)	0.614	0.585	0.826	0.837	0.849
λ_F (μm)	0.658	0.660	0.511	0.654	0.653
λ_G (μm)	0.379	0.385	0.372	0.358	0.376
Film Thickness (μm)	0.432	0.439	0.453	0.360	0.388
Substrate Thickness (μm)	1240	1240	1240	1240	1240
White loss	0.002	0.002	-0.03	0.007	0.003
Relative Error	1.169×10^{-3}	1.707×10^{-3}	1.392×10^{-3}	1.31×10^{-3}	1.270×10^{-3}

Fig. 10 $\text{Zn}_{0.99-x}\text{Co}_{0.01}\text{Ce}_x\text{O}$ ($x = 0.00\text{--}0.05$) thin films: extinction coefficient vs. λ 

Equation (14) can be stated differently as $(F(R_\alpha)h\nu)^2 = k^2(h\nu - E_g)$. A linear fit was used to approximate the $(F(R_\alpha)h\nu)^2$ graph's slope. As shown in Table 3 and Fig. 12a–f, the bandgap energy reached a minimum value of 3.272 eV for a Ce concentration of 1% and a maximum value of 3.277 eV for a Ce concentration of 4%. The optical bandgap of

the thin films exhibited fluctuations as the Ce content increased. This behavior can be attributed to the possible substitution of Zn ions by Ce ions in the ZnO lattice. The observed bandgap energies are consistent with the findings of Karakaya and Kaya [8].

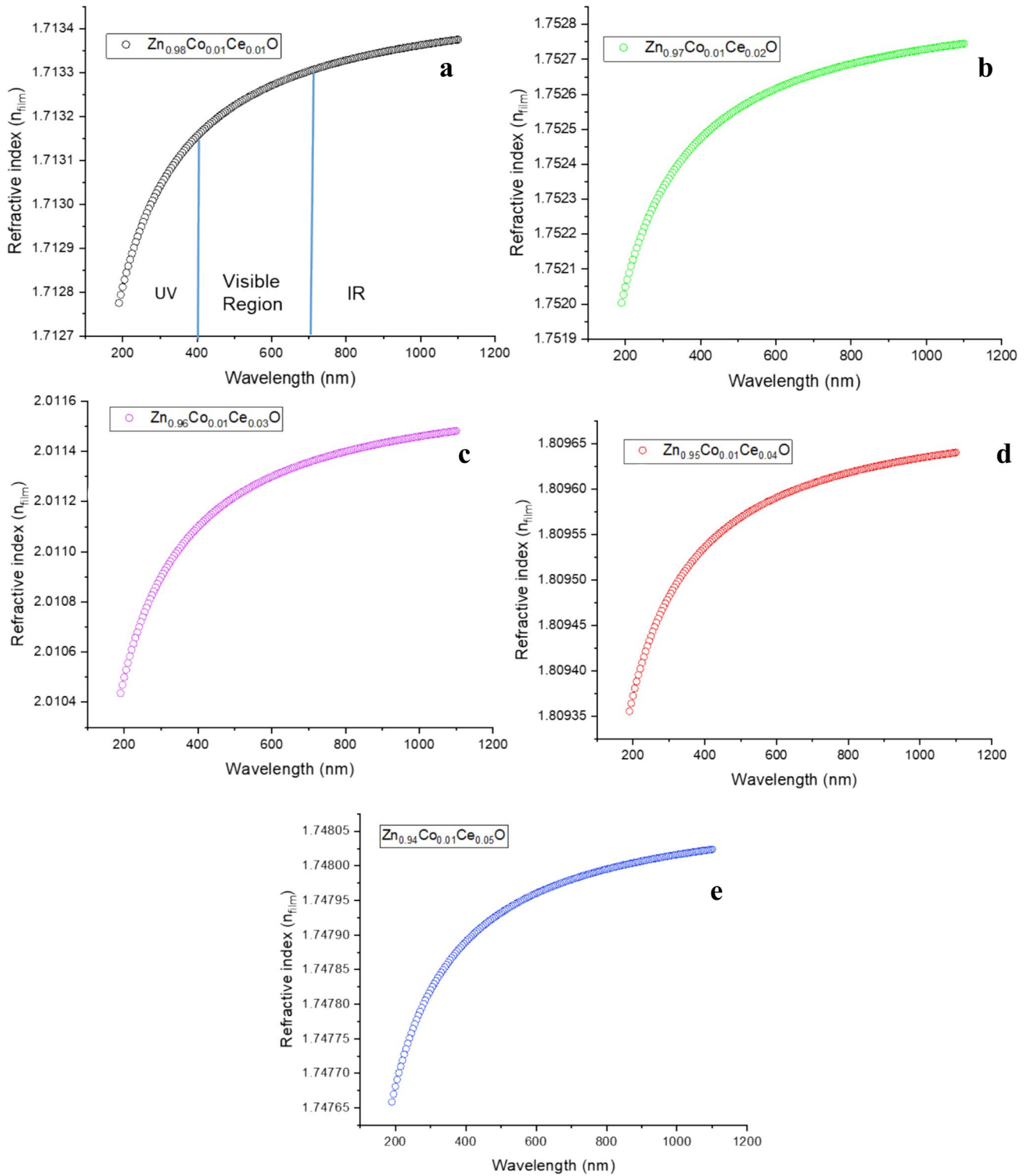


Fig. 11 $Zn_{0.99-x}Co_{0.01}Ce_xO$ ($x = 0.01-0.05$) thin films: refractive index vs. λ

Table 3 Fitting curve function $y(h\nu) = A \times h\nu + B$, band gap energies E_g and variances σ^2 for different Ce doping ratios for the $\text{Zn}_{0.99-x}\text{Co}_{0.01}\text{Ce}_x\text{O}$ thin films

x	A	B	$E_g(\text{eV})$	σ^2
0.01	47.66	-156.05	3.274	2.45×10^{-3}
0.02	49.60	-162.53	3.277	2.89×10^{-3}
0.03	48.42	-158.58	3.275	2.69×10^{-3}
0.04	47.33	-155.04	3.276	2.27×10^{-3}
0.05	45.93	-150.28	3.272	1.94×10^{-3}

3.7 The calculation of urbach energy

In Fig. 13, the photon energy $h\nu$ (in eV) is plotted against the logarithm of the absorption coefficient for $\text{Zn}_{0.99-x}\text{Co}_{0.01}\text{Ce}_x\text{O}$ ($x = 0.01\text{--}0.05$) thin films. The relationship between the absorption coefficient (α) and photon energy ($h\nu$) near the band gap is described by Urbach's law, which states that the absorption coefficient exhibits an exponential dependence on photon energy, as expressed by the following relation:

$$\alpha = \alpha_0 e^{h\nu/E_u} \quad (15)$$

where α_0 is a constant and E_u is the Urbach energy, which represents the impact of all potential faults and is a measure of structural disorder and defect density [39].

The following connection is used to estimate the Urbach energy E_u values near the band gap, which are connected to the band gap's localized states' width:

$$E_u = \left[\frac{d(\ln \alpha)}{d(h\nu)} \right]^{-1} \quad (16)$$

where α is the absorption coefficient and $h\nu$ is the photon energy [16]. However, since only tabular values of the absorption coefficient are available, we estimated the first derivative of $\ln \alpha$ with respect to the photon energy ($h\nu$) using two distinct finite difference techniques: the 3-point central and 5-point formulae.

These approximations provide second-order and fourth-order accuracy, respectively. The Urbach energy values E_u at E_g were evaluated by plotting the bandgap values as a function of Ce concentration (x) for ZnCoCeO thin films, as listed in Table 4 and shown

in Fig. 14. The Urbach energy values (E_u) show a non-monotonic dependence on Ce concentration as shown in Table 4, indicating complex doping-induced modifications to the film's electronic structure [44, 45]. As shown in Fig. 14, doping with Ce reduced the Urbach energy (E_u) of $\text{Zn}_{0.99-x}\text{Co}_{0.01}\text{Ce}_x\text{O}$ films, except for the 2% Ce concentration. The decrease in E_u indicates an increase in structural disorder and defect density as the Ce concentration in $\text{Zn}_{0.99-x}\text{Co}_{0.01}\text{Ce}_x\text{O}$ films increased. For the 2% Ce concentration, the highest Urbach energy value was approximately 1550 meV according to 5-point F.D.M.. In contrast, Bindu and Thomas [46] reported an E_u value of 490 meV for undoped ZnO thin films. This suggests that doping with Ce increases the Urbach energy value of $\text{Zn}_{0.99-x}\text{Co}_{0.01}\text{Ce}_x\text{O}$. A larger E_u indicates higher structural disorder (e.g., vacancies). The elevated Urbach energy value can be attributed to the formation of additional interband states between the valence and conduction bands. The Urbach energy value becomes minimum at 0.05% Ce which could optimize film performance (e.g., solar cells, sensors). Moreover, it also reflects improved crystallinity and reduced defect states, implying optimal Ce doping enhances structural ordering. The peak value of the Urbach energy at 0.01% Ce aligns with expectations for high defect density in low-doping regimes, typical of sol-gel synthesis. Lower E_u values (e.g., 0.02–0.05% Ce) correlate with reduced band-tail states, beneficial for optoelectronic applications (e.g., higher carrier mobility) [44, 45].

4 Conclusion

The c-axis-oriented (002) hexagonal wurtzite $\text{Zn}_{0.99-x}\text{Co}_{0.01}\text{Ce}_x\text{O}$ ($x = 0.00\text{--}0.05$, in increments of 0.01) thin films were fabricated as a single-phase material using the sol-gel process, and their optical properties were determined using the DFCS model [36]. We found that the film thicknesses ranged from 350 to 455 nm. The refractive index exhibited an increasing trend, with values ranging from 1.71 to 2.02.

We found that the Ce-doped $\text{Zn}_{0.99-x}\text{Co}_{0.01}\text{Ce}_x\text{O}$ thin films exhibited optical bandgap energy values ranging from 3.272 to 3.277 eV, with the minimum occurring at 1% Ce concentration and the maximum at 4% Ce concentration. The highest Urbach energy value was observed at a Ce concentration of 2%.

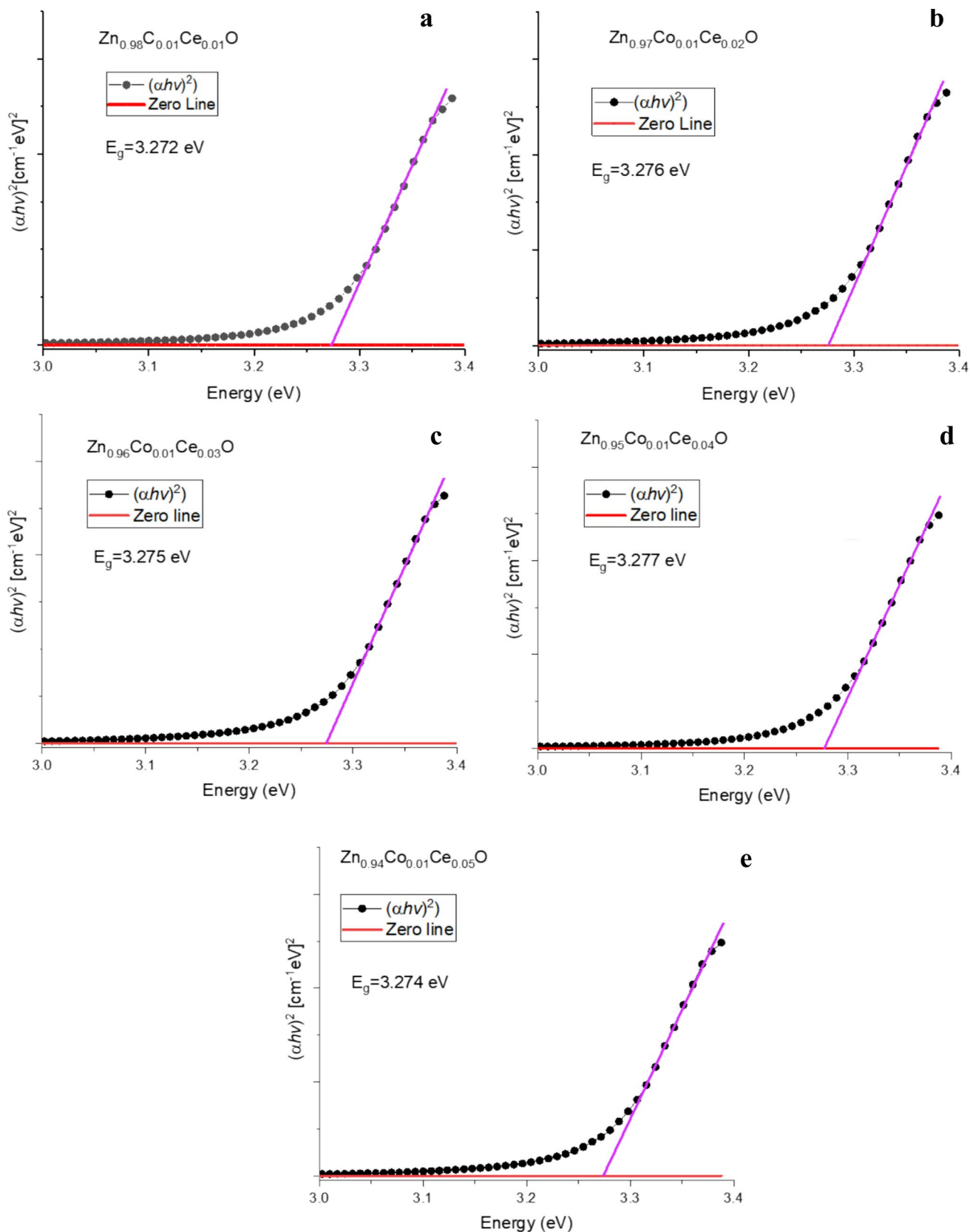


Fig. 12 The plots of $(\alpha h\nu)^2$ as a function of photon energy ($h\nu$) and the linear fit for the $\text{Zn}_{0.99-x}\text{Co}_{0.01}\text{Ce}_x\text{O}$ **a** $x = 0.01$, $E_g = 3.272$ eV, **b** $x = 0.02$, $E_g = 3.276$ eV, **c** $x = 0.03$, $E_g = 3.275$ eV, **d** $x = 0.04$, $E_g = 3.277$ eV, and **e** $x = 0.05$, $E_g = 3.274$ eV

Fig. 13 $\ln \alpha$ versus photon energy $h\nu$ (eV) of $Zn_{0.99-x}Co_{0.01}Ce_xO$ ($x = 0.01-0.05$) thin films

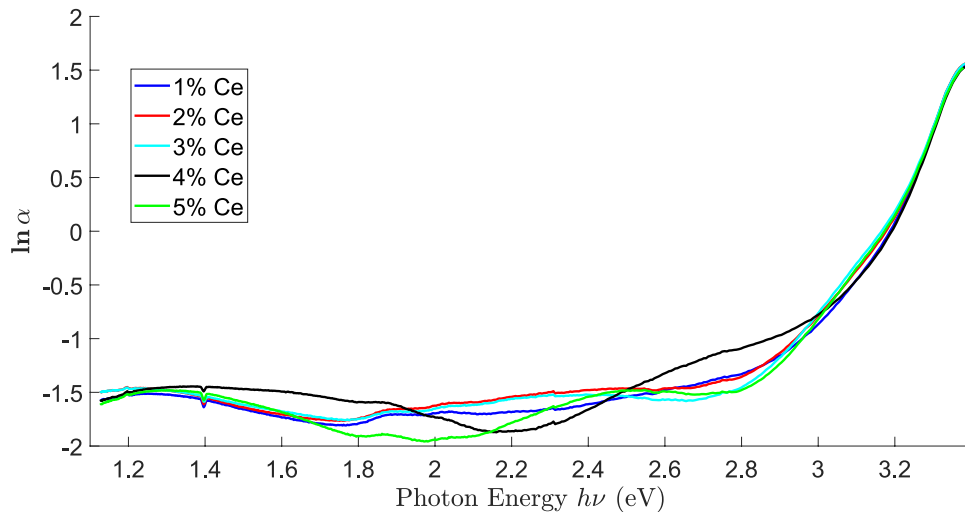
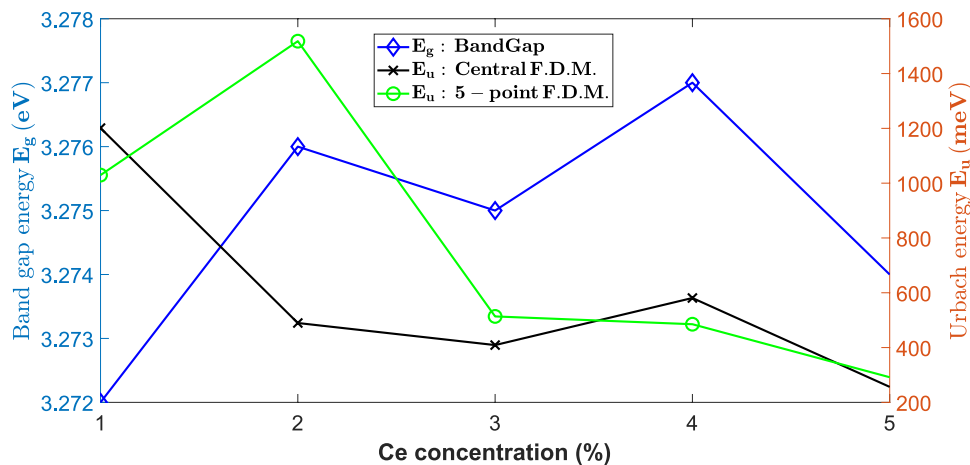


Table 4 The Urbach energy values E_u in meV for the $Zn_{0.99-x}Co_{0.01}Ce_xO$ ($x=0.01-0.05$) thin films computed at E_g using two finite difference methods (F.D.M.)

Ce concentration	3-point Central F.D.M. (meV)	5-point F.D.M. (meV)
0.01	1201.05	1029.47
0.02	489.64	1518.14
0.03	409.07	513.64
0.04	580.89	485.18
0.05	256.51	291.71

The refractive index and bandgap energy values obtained for Co/Ce-doped ZnO thin films highlight their potential for various optoelectronic applications. The values measured in both the visible and infrared (IR) regions make these films suitable for use in solar cells, LEDs, sensors, and photodetectors. As a result, they could play a critical role in enhancing the efficiency of optoelectronic devices.

Fig. 14 The 3-point central and 5-point finite difference methods (FDM) of $Zn_{0.99-x}Co_{0.01}Ce_xO$ ($x = 0.00-0.05$) thin films are two distinct finite difference approaches that estimate the band gap E_g as a function of Ce concentration (x) and Urbach energy (E_u) values



Acknowledgements

This research was supported by the Research Fund of Bahcesehir University under Project No: BAP-2021.01.27, Istanbul, Turkiye. The authors extend their gratitude to all individuals who have contributed to this research but were not mentioned individually. Your support is an integral part of this study.

Author contributions

All authors contributed to the study conception and design. Material preparation, data collection, and analysis were performed by Lutfi Arda and Ersin Ozugurlu. All authors read and approved the final manuscript.

Funding

Open access funding provided by the Scientific and Technological Research Council of Türkiye (TÜBİTAK). This research was supported by the Research Fund of Bahcesehir University under Project No: BAP-2021.01.27, Istanbul, Turkiye.

Data availability

Data will be made available on request.

Declarations

Conflict of interest The authors declare that they have no known conflict financial interests or personal relationships that could have appeared to influence the work reported in this paper.

Open Access This article is licensed under a Creative Commons Attribution 4.0 International License, which permits use, sharing, adaptation, distribution and reproduction in any medium or format, as long as you give appropriate credit to the original author(s) and the source, provide a link to the Creative Commons licence, and indicate if changes were made. The images or other third party material in this article are included in the article's Creative Commons licence, unless indicated otherwise in a credit line to

the material. If material is not included in the article's Creative Commons licence and your intended use is not permitted by statutory regulation or exceeds the permitted use, you will need to obtain permission directly from the copyright holder. To view a copy of this licence, visit <http://creativecommons.org/licenses/by/4.0/>.

References

1. R. Mariappan, V. Ponnuswamy, P. Suresh, R. Suresh, M. Ragavendar, A.C. Bose, Nanostructured $Ce_xZn_{1-x}O$ thin films: influence of Ce doping on the structural, optical and electrical properties. *J. Alloys Compd.* **588**, 170–176 (2014)
2. A. Chelouche, T. Touam, M. Tazerout, F. Boudjouan, D. Djouadi, A. Doghmane, Low cerium doping investigation on structural and photoluminescence properties of sol-gel ZnO thin films. *J. Lumin.* **181**, 448–454 (2017)
3. K. Karthik, S. Dhanuskodi, C. Gobinath, S. Prabukumar, S. Sivaramkrishnan, Photocatalytic and antibacterial activities of hydrothermally prepared CdO nanoparticles. *J. Mater. Sci. Mater. Electron.* **28**, 11420–11429 (2017)
4. N. Narayanan, N.K. Deepak, Realizing luminescent downshifting in ZnO thin films by Ce doping with enhancement of photocatalytic activity. *Solid State Sci.* **78**, 144–155 (2018)
5. M.R. Prasad, M. Haris, M. Sridharan, NH₃ sensing properties of surface modified Ce-doped nanostructured ZnO thin films prepared by spray pyrolysis method. *Sensor. Actuator.* **269**, 435–443 (2018)
6. R.A. Zargar, A.H. Shah, M. Arora, Crystallographic, spectroscopic and electrical study of ZnO:CdO nanocomposite-coated films for photovoltaic applications. *Arab. J. Sci. Eng.* **44**, 6631–6636 (2019)
7. S. Choudhary, M. Sharma, V. Krishnan, S. Mohapatra, Facile synthesis of Ce doped ZnO nanowires for efficient photocatalytic removal of organic pollutants from water. *Mater. Today Commun.* **34**, 105361 (2023)
8. S. Karakaya, L. Kaba, Nanoflower-like cerium-doped ZnO photocatalyst deposited by spray pyrolysis for the degradation of methylene blue dye. *Mater. Today Sustain.* **27**, 100875 (2024)
9. S. Karakaya, L. Kaba, Photocatalytic activity of rare earth elements (Gd and Ce) co-doped ZnO nanostructured films. *Ceram. Int.* **50**(17), 30743–30753 (2024)

10. D.T.B. Hop, T.Q. Tuan, N.V. Quang, N. Tu, H. Le Tien, M.T. Tran, T.Q. Vinh, N.C. Tu, T.N. Bach, V.D. Dao, P.T.L. Huong, Enhanced visible-light photocatalytic degradation efficiency of Ce³⁺-doped ZnO nanoparticles synthesized by sol-gel method. *Ceram. Int.* **50**, 17338–17353 (2024)
11. P. Pascariu, C. Cojocaru, V. Ciornea, C. Romanitan, A.B. Serban, Visible lightresponsive Ce-doped ZnO ceramic nanostructures as effective photocatalysts for removal of persistent organic pollutants from contaminated waters. *Mater. Today Sustain.* **26**, 100719 (2024)
12. S. Ozharar, D. Akcan, L. Arda, Determination of the refractive index and the thickness of double side coated thin films. *J. Optoelectron. Adv. M.* **18**(1–2), 65–69 (2016)
13. A. Chelouche, T. Touam, M. Tazerout, D. Djouadi, F. Boudjouan, Effect of Li co doping on highly oriented sol-gel Ce-doped ZnO thin films properties. *J. Lumin.* **188**, 331–336 (2017)
14. A. Kumawat, S. Chattopadhyay, R.D.K. Misra, K.P. Misra, U. Valiyaneerilakkal, Significance of microstrain in impacting band gap and photoluminescence behavior of Ce-doped ZnO thin films deposited via sol-gel process. *Phys. Scr.* **98**(2), 025816 (2023)
15. M. El Jouad, M. Alaoui Lamrani, Z. Sofiani, M. Addou, T. El Habbani, N. Fellahi, K. Bahedi, L. Dghoughi, A. Monteil, B. Sahraoui, S. Dabos, N. Gaumer, Roughness effect on photoluminescence of cerium doped zinc oxide thin films. *Opt. Mater.* **31**, 1357–1361 (2009)
16. R. Vettumperumal, S. Kalyanaraman, B. Santoshkumar, R. Thangavel, Estimation of electron-phonon coupling and Urbach energy in group-I elements doped ZnO nanoparticles and thin films by sol-gel method. *Mater. Res. Bull.* **77**, 101–110 (2016)
17. S. Ghosh, U.M.K. Kumar, B.N.S. Bhaktha, Heat-treatment controlled structural and optical properties of sol-gel fabricated Eu: ZnO thin films. *Opt. Mater.* **64**, 288–294 (2017)
18. E. Asikuzun, O. Ozturk, L. Arda, C. Terzioglu, Microstructural and electrical characterizations of transparent Er-doped ZnO nano-thin films prepared by sol-gel process. *J. Mater. Sci. Mater. Electron.* **28**, 14314–14322 (2017)
19. L. Wang, Z. Ji, J. Lin, P. Li, Preparation and optical and photocatalytic properties of Ce-doped ZnO microstructures by simple solution method. *Mater. Sci. Semicond. Process.* **71**, 401–408 (2017)
20. D. Akcan, A. Gungor, L. Arda, Structural and optical properties of Na-doped ZnO films. *J. Mol. Struct.* **1161**, 299–305 (2018)
21. M. Tosun, L. Arda, Effect of temperature and film thickness on structural and mechanical properties of c-axis oriented Zn_{0.95}Mg_{0.05}O thin films. *Ceram. Int.* **45**, 16234–16243 (2019)
22. Y. Pepe, A. Karatay, Y.O. Donar, A. Sınağ, H. Unver, A. Elmali, Tuning the energy bandgap and nonlinear absorption coefficients of CdO nanocomposite films with doping and annealing process. *Opt. Mater.* **103**, 109880 (2020)
23. Y. Pepe, S. Akkoyun, B. Bozkurt, A. Karatay, A. Ates, A. Elmali, Investigation of the wavelength dependent nonlinear absorption mechanisms of polyvinylpyrrolidone and cadmium selenide hybrid nanofibers. *Opt. Laser Technol.* **164**, 109497 (2023)
24. Y. Pepe, S. Akkoyun, N. Asci, E. Cevik, Y. Tutel, A. Karatay, H.E. Unalan, A. Elmali, Investigation of the defect and intensity-dependent optical limiting performance of MnO₂ nanoparticle-filled polyvinylpyrrolidone composite nanofibers. *ACS Omega* **8**(50), 47954–47963 (2023)
25. P. Priyadarshini, S.P. Panda, A. Parida, R. Naik, Microwave assisted synthesis of ZnIn₂S₄ nanoparticles: effect of power variation for photoresponse and optoelectronic applications. *Dalton Trans.* **53**(34), 14481–14495 (2024)
26. P. Priyadarshini, P. Rout, S. Supriya, P.C. Kumar, R. Naik, Effect of Cu concentration on optimizing the optical, morphological, and structural characteristics of ZnIn₂S₄ nanosheets for photoresponse applications. *ACS Appl. Nano Mater.* **7**(24), 28131–28144 (2024)
27. B.B. Tripathy, J. Das, D.K. Mishra, R. Naik, S.N. Sarangi, P. Kumar, K. Satpathy, Microscopic and spectroscopic behavior of ZnO@ MWCNTs composite. *J. Mater. Sci. Mater. Electron.* **36**(2), 145 (2025)
28. V. Anand, A. Sakthivelu, K.D. Arun Kumar, S. Valanarasu, V. Ganesh, M. Shkir, A. Kathalingam, S. AlFaify, Novel rare earth Gd and Al co-doped ZnO thin films prepared by nebulizer spray method for optoelectronic applications. *Superlatt. Microst.* **123**, 311–322 (2018)
29. M. Soylu, M. Coskun, Controlling the properties of ZnO thin films by varying precursor concentration. *J. Alloys Compd.* **741**, 957–968 (2018)
30. G. Flores-Carrasco, M. Rodríguez-Pena, A. Urbieta, P. Fernandez, M. Eugenia Rabanal, ZnO nanoparticles with controllable Ce content for efficient photocatalytic degradation of MB synthesized by the polyol method. *Catalysts* **11**, 71 (2021)
31. F. Boufelgha, N. Brihi, F. Labreche, H. Guendouz, A. Barbadj, Enhanced of blue and green emission by Ce–ZnO thin films prepared by sol–gel technique. *Semiconductors* **56**(4), 275–280 (2022)
32. A. Amri, Z.T. Jiang, T. Pryor, C.Y. Yin, Z. Xie, N. Mondinos, Optical and mechanical characterization of novel cobalt-based metal oxide thin films synthesized using sol-gel dip-coating method. *Surf. Coating. Technol.* **207**, 367–374 (2012)

33. S. Satpathy, U. Panigrahi, R. Biswal, P. Mallick, Investigation on the microstructural, optical and magnetic properties of Ce doped ZnO nanorods. *Materialia* **25**, 101536 (2022)
34. M. Xin, Crystal structure and optical properties of ZnO: Ce nano film. *Molecules* **27**, 5208 (2022)
35. P. Singh, R. Kumar, R.K. Singh, Fabrication of Co- and Ce-doped ZnO nanoparticles: a structural, morphological and optical properties investigation. *Appl. Nanosci.* **10**, 1231–1241 (2020)
36. D. Akcan, S. Ozharar, E. Ozugurlu, L. Arda, The effects of Co/Cu Co-doped ZnO thin films: An optical study. *J. Alloys Compd.* **797**, 253–261 (2019)
37. H. He, F. Zhuge, Z. Ye, L. Zhu, F. Wang, B. Zhao, J. Huang, Strain and its effect on optical properties of Al–N codoped ZnO films. *J. Appl. Phys.* **99**, 023503 (2006)
38. K. Senturk, B. Yalcin, I.E. Yalcin, M.C. Alphan, M.S. Sengul, C. Tav, U. Yahsi, L. Arda, The role of defects in the structural and photocatalytic properties of Mg/B co-doped ZnO nanoparticles. *J. Mater. Sci. Mater. Electron.* **34**, 847 (2023)
39. L. Arda, O. Karatas, M.C. Alphan, E. Ozugurlu, Electron spin resonance and photoluminescence and studies of Co/Mg co-doped ZnO nanoparticles. *Int. J. Appl. Ceram. Technol.* **21**(3), 2458–2473 (2024)
40. L. Arda, Z. Raad, S. Veziroglu, C. Tav, U. Yahsi, The influence of defects on the structural, optical, and antibacterial properties of Cr/Cu Co-doped ZnO nanoparticles. *J. Mol. Struct.* **1320**, 139663 (2025)
41. A. Parida, D. Sahoo, D. Alagarasan, S. Vardhrajperumal, R. Ganesan, R. Naik, Increase in nonlinear susceptibility and refractive index in quaternary In₁₅Sb₁₀S₁₅Se₆₀ thin films upon annealing at different temperature for photonic applications. *J. Alloy. Compd.* **905**, 164143 (2022)
42. S.K. Abdel-Aal, G. Kocher-Oberlehner, A. Ionov, R.N. Mozhchil, Effect of organic chain length on structure, electronic composition, lattice potential energy, and optical properties of 2D hybrid perovskites [(NH₃)(CH₂)_n(NH₃)]CuCl₄, n= 2–9. *Appl. Phys. A* **123**, 1–10 (2017)
43. S.K. Abdel-Aal, A.S. Abdel-Rahman, Fascinating physical properties of 2D hybrid perovskite [(NH₃)(CH₂)₇(NH₃)]CuCl_xBr_{4-x}, x= 0, 2 and 4. *J. Electron. Mater.* **48**, 1686–1693 (2019)
44. R. Naik, S.K. Parida, C. Kumar, R. Ganesan, K.S. Sannuni, Optical properties change in Sb₄₀S₄₀Se₂₀ thin films by light-induced effect. *J. Alloy. Compd.* **522**, 172–177 (2012)
45. R. Naik, S. Jena, R. Ganesan, N.K. Sahoo, Photo-induced optical bleaching in Ge₁₂Sb₂₅S₆₃ amorphous chalcogenide thin films: effect of 532 nm laser illumination. *Laser Phys.* **25**(3), 036001 (2015)
46. P. Bindu, S. Thomas, Optical properties of ZnO nanoparticles synthesized from a polysaccharide and ZnCl₂. *Acta Phys. Pol A.* **131**, 1474–1478 (2017)

Publisher's Note Springer Nature remains neutral with regard to jurisdictional claims in published maps and institutional affiliations.